A scintillator-based range telescope for particle therapy

IOP Publishing Phys. Med. Biol. 65 (2020) 165001 https://doi.org/10.1088/1361-6560/ab9415

Physics in Medicine & Biology

IPEM Institute of Physics and Engineering in Medicine

A scintillator-based range telescope for particle therapy

Laurent Kelleter[1], Raffaella Radogna[1], Lennart Volz[2,3], Derek Attree[1], Anastasia Basharina-Freshville[1], Joao Seco[2,3], Ruben Saakyan[1] and Simon Jolly[1]

[1] Dept. Physics and Astronomy, University College London, Gower Street, WC1E 6BT London, United Kingdom
[2] Department of Biomedical Physics in Radiation Oncology, German Cancer Research Center (DKFZ), Heidelberg, Germany
[3] Department of Physics and Astronomy, Heidelberg University, Heidelberg, Germany

E-mail: laurent.kelleter@ucl.ac.uk

Keywords: pencil beam range, quality assurance, scintillator, CMOS sensor, Bragg curve, light quenching

OPEN ACCESS

RECEIVED
5 March 2020

REVISED
29 April 2020

ACCEPTED FOR PUBLICATION
18 May 2020

PUBLISHED
10 August 2020

Abstract

The commissioning and operation of a particle therapy centre requires an extensive set of detectors for measuring various parameters of the treatment beam. Among the key devices are detectors for beam range quality assurance. In this work, a novel range telescope based on a plastic scintillator and read out by a large-scale CMOS sensor is presented. The detector is made of a stack of 49 plastic scintillator sheets with a thickness of 2–3 mm and an active area of 100×100 mm^2, resulting in a total physical stack thickness of 124.2 mm. This compact design avoids optical artefacts that are common in other scintillation detectors. The range of a proton beam is reconstructed using a novel Bragg curve model that incorporates scintillator quenching effects. Measurements to characterise the performance of the detector were carried out at the Heidelberger Ionenstrahl-Therapiezentrum (HIT, Heidelberg, GER) and the Clatterbridge Cancer Centre (CCC, Bebington, UK). The maximum difference between the measured range and the reference range was found to be 0.41 mm at a proton beam range of 310 mm and was dominated by detector alignment uncertainties. With the new detector prototype, the water-equivalent thickness of PMMA degrader blocks has been reconstructed within $\pm$ 0.1 mm. An evaluation of the radiation hardness proves that the range reconstruction algorithm is robust following the deposition of 6,300 Gy peak dose into the detector. Furthermore, small variations in the beam spot size and transverse beam position are shown to have a negligible effect on the range reconstruction accuracy. The potential for range measurements of ion beams is also investigated.

1. Introduction

Particle therapy is a form of highly targeted radiation therapy that is used to treat certain types of cancer. It has seen a boom in the past two decades with more than ninety centres being operational worldwide as of 2019 — most of which are proton therapy centres—and more facilities being in the construction or planning phase (Particle Therapy Co-Operative Group 2019). The key advantage of particle therapy, relative to conventional photon radiotherapy, is the characteristic dose distribution through the patient with a low entrance dose that increases to a maximum—the Bragg peak—beyond which very little dose is deposited. This enables the tumour to be targeted with greater precision than in photon radiotherapy. The healthy tissue surrounding the tumour can therefore be spared more effectively (Kristensen *et al* 2015). Due to the large dose gradient it is essential for a safe and effective treatment to know the exact location of the Bragg peak. A significant amount of time is therefore dedicated to measuring percent depth-dose curves (PDD) that characterise the longitudinal dose distribution of the particle beam—and therefore the precise depth of the Bragg peak—during both the commissioning of the centre (Gillin *et al* 2010) and regular quality assurance during clinical operation (Grevillot *et al* 2018, Actis *et al* 2017, Rana *et al* 2019).

The gold standard for measuring reference PDD curves are ionisation chambers that are immersed in a water tank in order to scan the pencil beam at different depths and transverse positions (Karger *et al* 2010). Such water phantoms are used for dosimetry as well as for beam range measurements. However, scanning the PDD curve by moving the ionisation chamber along the Bragg curve is time consuming and can take several minutes for a single pencil beam. Many centres therefore use faster detectors for beam range measurements,

such as Multi-Layer Ionisation Chambers (MLIC) (Actis *et al* 2017). However, they suffer from different drawbacks: ionisation chambers are not inherently water-equivalent and need to be sandwiched with suitable absorber material such that the MLIC measures water-equivalent thickness (WET). Also, the finite size of their charge-collecting electrodes complicates the measurement of integrated depth-dose curves (Baeumer *et al* 2015) which is why commercial MLICs (e.g. from IBA Dosimetry, Schwarzenbruck, Germany) are available with differently sized electrodes for the measurement of either large (IBA Zebra) or small (IBA Giraffe) fields. Furthermore, ionisation chambers exhibit dose-rate effects (Karsch *et al* 2012) and need to be cautiously recalibrated when used outside of reference conditions (Karger *et al* 2010). Finally, the analogue electronics used in the charge collection and measurement can make MLICs fragile and susceptible to damage if not handled carefully.

In the absence of ideal instrumentation for particle beam measurements, alternative detector systems based on scintillating materials have been investigated by several groups in order to complement ionisation chambers (Beaulieu and Beddar 2016). A scintillator is a material that emits light in response to the deposition of energy by ionising radiation. Organic scintillators are composed of a synthetic polymer base such as polystyrene (PS) or polyvinyl toluene (PVT), a primary dopant that converts the UV radiation of the base into visible light and a secondary dopant that acts as a wavelength shifter (Knoll 1979). The latter ensures that the scintillator is transparent to its own scintillation light. Organic scintillators exhibit multiple characteristics that make them interesting for applications in particle therapy detectors such as the low price, fast signal rise time, scalability, dose-rate independence and nearly water-equivalent density (Knoll 1979).

Historically, scintillators have been avoided for reference dosimetry in particle therapy because they suffer from radiation damage and exhibit light quenching effects. The light quenching leads to a non-linear dependence between light output and dose deposition for particles with high energy losses (linear energy transfer, LET) such as protons (Birks 1951). However, scintillating screens are commonly used for beam spot position (Russo *et al* 2017) and field homogeneity measurements (Karger *et al* 2010). Moreover, scintillating screens have successfully been employed for Percent Depth-Light curve (PDL) measurements in water phantoms (Boon *et al* 1998, Hoehr *et al* 2018). Fukushima *et al* suggested using a block of plastic scintillator and a commercial digital camera for the fast acquisition of PDL curves (Fukushima *et al* 2006). This idea was further developed by other groups (Almurayshid *et al* 2017, Mazzucconi *et al* 2018). Moreover, a detector based on liquid scintillator for fast quasi-3D pencil beam measurements was developed at M.D. Anderson Cancer Center (Houston, Texas, USA) (Beddar *et al* 2009, Archambault *et al* 2012, Darne *et al* 2018). However, all these devices have in common that they have to correct for optical artefacts that come with the use of a digital camera to record the light output (Robertson *et al* 2014). In addition, complex high-resolution simulations of the LET distribution in the scintillator are necessary in order to correct for quenching effects (Robertson *et al* 2013, Alsanea *et al* 2020).

A novel range telescope based on a stack of thin sheets of plastic scintillator is under development at University College London (UCL, London, UK). The evaluation of a prototype detector is presented in this work. The application of the detector focuses on the range measurement of particle pencil beams, similar to a MLIC. The scintillation light is read out with a large-scale CMOS sensor which is directly coupled to the scintillator stack. This configuration avoids optical artefacts and allows a very compact detector design. The light quenching is not corrected for in the detector itself but is accounted for by utilising a new model of a quenched Bragg curve which was found to reconstruct the proton beam range within $\pm$ 0.16 mm (Kelleter and Jolly 2020).

2. Materials and methods

2.1. Scintillator

The range telescope has a segmented design using 49 thin scintillator sheets with a transverse area of 100×100 mm^2 and a thickness between 2 and 3 mm: the schematic design is shown in figure 1(a). The transverse sheet size ensures that the majority of the dose from a conventional therapeutic proton pencil beam is absorbed in the scintillator, whereas the sheet thickness is a compromise between required spatial resolution and mechanical stability.

The sheets are composed of a polystyrene-based scintillator (Nuvia a.s. Třebíč, Czech Republic) with a density of 1.03 ± 0.01 g cm^{-3}, a decay constant of 2.5 ns and a light output of 56% of that of anthracene (NuviaTech Instruments 2019). Each sheet is sprayed with a thin layer—between 0.01-0.07 mm per sheet—of matt black spray paint (Halfords, Redditch, UK) in order to ensure optical decoupling. Two side orthogonal faces of each sheet were left unpainted to allow the scintillation light to emerge and be simultaneously measured with different devices. The top face was coupled to the CMOS sensor and the light from the second unpainted face was recorded with a DSLR camera. The results of the latter readout device are not shown in this work. The density of the dried paint film provided by the manufacturer is

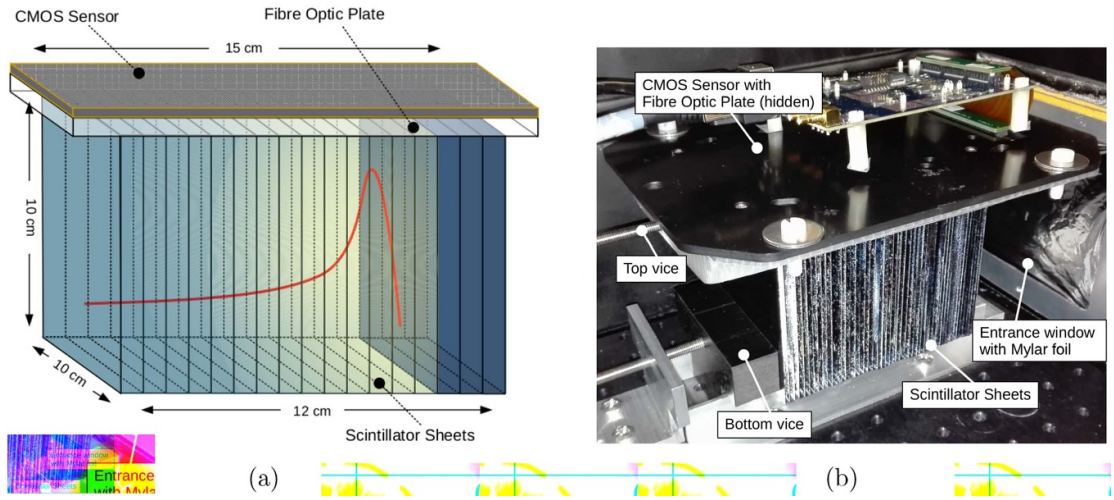

Figure 1. (a) Sketch and (b) photograph of the prototype scintillator-based range telescope with thin scintillator sheets and a CMOS sensor readout.

1.231 g cm^{-3}. The thickness of all painted scintillator sheets was measured individually at room temperature at eight points around the sheet with a micrometer screw gauge. The physical thickness of the full scintillator sheet stack is 124.20 mm, giving an average sheet thickness of 2.53 mm. The average standard deviation of the sheet thickness is 0.02 mm. The uncertainty on the physical thickness of the whole stack due to thermal expansion is calculated to be smaller than $\pm$ 0.02 mm (Subrahmanyam and Subramanyam 1987). The water equivalent thickness of the painted scintillator stack was determined by measuring the range pull-back of a carbon ion beam (270 MeV/u) with a Peakfinder (PKF) water column (PTW, Freiburg, Germany) and found to be 127.27$\pm$ 0.04 mm. The WET was also measured with a proton and a helium beam and the measured values agreed within the measurement uncertainty (0.04 mm). The displaced air was taken into account in the calculation of the WET.

2.2. CMOS sensor

A large-scale CMOS image sensor (ISDI, London, UK) is used for the detection of the scintillation light output. The sensor has an active area of 153.6 $\times$ 103.0 mm^2, a pixel size of 0.1 $\times$ 0.1 mm^2 and a resolution of 1536 $\times$ 1030 pixels: each of the 1536 rows has a length of 1030 pixels. The sensor is operated in rolling-shutter mode, i.e. the sensor is read out row by row. Two pixel rows are read out simultaneously. The readout of a pixel row pair takes 0.02 ms during which no charge is accumulated (dead time). The frame rate of the sensor is 25 frames per second (fps). This makes the total acquisition time per frame 40 ms of which readout takes 15 ms. The minimum delivery time of a pencil beam is therefore 15 ms.

Image frames are transferred via a Camera Link cable to a PIXCI 10^{-8} PCI Express (PCIe) x8 Frame Grabber (EPIX Inc. Buffalo Grove, Illinois, USA). The PCIe card is inserted in a PCIe x16 Expansion Chassis (StarTech.com, Lockbourne, Ohio, USA) that is connected to a computer with a Thunderbolt 3 cable. The images are saved using the software XCAP-Lite v3.8 for Windows (EPIX Inc.), which comes with the PCIe card. A maximum of 21 full resolution images can be taken with the XCAP-Lite software which results in a total acquisition time of 840 ms. However, the number of frames and therefore the maximum acquisition time can be increased by decreasing the number of pixels to be read out. This allows fields to be recorded that take longer to be delivered than 840 ms, e.g. spread-out Bragg peaks (SOBP). The sensitivity of the sensor can be adjusted by changing between low and high full-well mode, providing an adjustment in dynamic range and sensitivity by a factor of 5.73. The sensor was operated in high full-well mode because of its superior linearity: deviations from a linear response to incoming light is $\pm$ 0.3% in high full-well mode versus $\pm$ 2% in low full-well mode. Each pixel has a 14 bit resolution (16, 384 counts) and a dark noise floor of $\sim$ 2, 500 counts. Before taking data, the sensor temperature was given about 15 minutes to stabilise. The remaining temperature dependence shows up as a constant offset along the pixel rows of up to 20 ADC counts. This offset is corrected in data analysis by matching the noise levels in the background image and in the region with no signal of the signal image. The uncertainty on this correction is estimated to be 5 ADC counts.

2.3. Range telescope

The scintillator sheet stack is held in place by a vice that is screwed to a Thorlabs optical breadboard inside a light-tight enclosure. The proton beam enters the scintillator stack perpendicular to the large face of the

scintillator sheets. The enclosure has two entrance windows on either end of the stack, each covered by four layers of aluminium-coated Mylar foil with a WET of ~ 0.03 mm. Light-tight feedthroughs are used for the USB connection and power supply to the CMOS sensor. The CMOS sensor itself is not directly exposed to the beam but is used for the readout of the scintillation light. For this, the image sensor is placed on top of the scintillator stack, fixed by a 3D-printed frame with a second integrated vice. A fibre-optic plate (ISDI) is used to protect the sensor and to couple it to the scintillator. No optical gel is used between the scintillator and image sensor since it was found not to improve the coupling. There is no need for a lens in between the stack and the image sensor due to the segmentation of the scintillator which allows the scintillation light to be attributed to a specific sheet.

The resulting range telescope is much more compact than detectors utilising a single monolithic block of scintillator, which normally require a digital camera placed up to a metre away from the scintillator to image the entire block (Fukushima *et al* 2006, Beddar *et al* 2009). Another advantage of this close-fitting setup is that a larger proportion of the light produced by the scintillator stack is collected and that there are no parallax effects that distort the image. As a consequence, the pixel-to-depth conversion is the same for every pixel such that the whole length of the range telescope can be used without the application of depth-dependent correction factors. Figure 1(a) shows a sketch of the resulting scintillator-based range telescope: a photograph of the resulting experimental setup is shown in figure 1(b).

2.4. Experimental setup

The experiments have been carried out in the experimental room of the Heidelberger Ionenstrahl-Therapiezentrum (HIT, Heidelberg, Germany), except for the radiation hardness assessment, which was performed at the Clatterbridge Cancer Centre (CCC, Bebington, UK). HIT uses a synchrotron to generate treatment beams of protons, helium, carbon or oxygen ions with ranges from 20 to 300 mm. As of January 2020, helium and oxygen ions are not yet available for patient treatment. CCC is a cyclotron-based facility with a fixed beam range of $R_0 = 31.13 \pm 0.20$ mm in water for ocular eye cancer treatment.

During the measurements the start of the scintillator stack was always placed in the beam isocentre in order to allow comparison with reference measurements. The detector alignment and positioning was performed using the in-house laser system and a spirit level. Remote control of the computer in the experimental cave was set up to manually trigger the data acquisition when the beam was on. PMMA slabs of known water-equivalent thickness were used to degrade the beam such that the Bragg peak of beams with a larger range than the total detector thickness could be imaged in the scintillator stack. The spill length at HIT was set to 5 s in order to leave enough time for the manual triggering of the image acquisition. The beam intensity at HIT was 1.2×10^9 protons per second.

At CCC, a brass collimator with a fixed circular opening diameter of 25 mm was used to collimate the double-scattered beam. The dose rate in the Bragg peak at CCC was 2 Gy s^{-1}.

2.5. Generation of a PDL curve

Each proton beam snapshot consists of 21 frames which are averaged in order to compensate for interplay effects between the rolling shutter readout and beam current fluctuations. Background correction is performed by subtracting a background image that was taken with identical measurement conditions but with the beam turned off. Figure 2(a) shows a raw image of a 106.17 MeV proton beam. It can be seen that the sensor has a faulty pixel cluster (white spot, middle left) and a faulty pixel row (white stripe, bottom). These artefacts are corrected for by the background subtraction. The two-dimensional image is then projected onto the beam axis for the generation of a depth-light curve.

In order to calibrate the light output of the scintillator, so-called 'shoot-through' curves are used. A shoot-through (ST) curve is a PDL curve of the highest available proton beam energy (222.71 MeV at HIT) as measured by the range telescope. A PMMA degrader of 5 cm thickness is placed in front of the stack in order to avoid the dose build-up region at the entrance of the Bragg curve (Kelleter *et al* 2019). This creates a relatively flat depth-dose curve in the scintillator stack. The ST measurement is performed from both sides of the scintillator stack in order to correct for the remaining slope in the Bragg curve plateau. The resulting averaged ST encodes all information about the coupling of each individual sheet to the CMOS sensor. A PDL curve is calibrated by performing a point-by-point division by the averaged ST curve.

A calibrated and an uncalibrated curve, after background subtraction, are shown in figure 2(b) for comparison. It can be seen that the calibration corrects for the variable coupling of the scintillator sheets and thus yields a smoother PDL curve. The calibration amplifies the noise in the region where there is no scintillator (pixel numbers 1–66 and 1310–1536): this is of no importance since these regions do not form part of the measurement volume and are ignored in further analysis.

The light coupling of the scintillator to the sensor varies along the readout face of the sheet. It is therefore important to use a shoot-through curve measured at the same transverse spot position and with the same

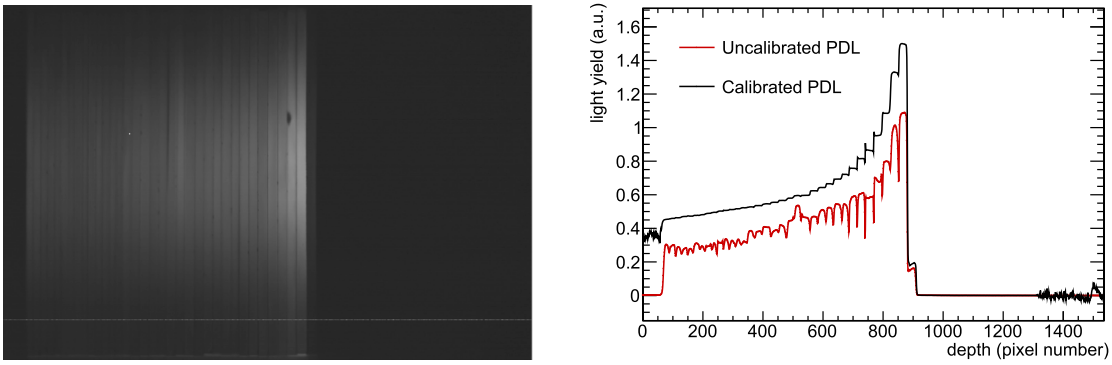

(a) Raw sensor image (b) Resulting PDL curve

Figure 2. (a) Raw image of the scintillation light output of a proton beam of 106.17 MeV in the range telescope. The beam travels from left to right. The scintillator starts at a depth of 67 pixels and ends at a depth of 1309 pixels. (b) Background-subtracted and projected PDL of the same measurement as in (a). Calibrated and uncalibrated PDL are shown for comparison.

spot size as the proton pencil beams for the calibration. The influence of the transverse beam spot position and size on the range measurement is discussed in section 3.3 and 3.4, respectively.

The pixel-to-depth conversion is performed by attributing a depth of zero to the pixel row at the start of the scintillator stack and a depth equivalent to the water-equivalent thickness of the whole stack to the last pixel row. The light output in each sheet is averaged and attributed to the water-equivalent depth at the centre of the respective sheet. During averaging, the light output within 0.5 mm of the edge of a sheet is neglected in order to reduce the influence of crosstalk. The uncertainty on the sheet light output is estimated by taking into account various effects: the beam widening along the path through the material (0.5% of light output), a beam spot size mismatch between the calibration ST and the PDL curve measurement (0.5%), the crosstalk between sheets (0.4% of light output in the neighbouring sheets) as well as sensor temperature differences between measurements (5 ADC counts).

2.6. Quenched Bragg curve

In order to measure the range of the proton beam, a 'quenched Bragg curve' (Kelleter and Jolly 2020) (QB) is fitted to the measured depth-light curve. The quenched Bragg curve is a combination of a model for a percent depth-dose curve by (Bortfeld 1997)f> and a model for quenching effects in plastic scintillator by (Birks 1951)f>. This model was specifically developed to enable the range reconstruction from PDL curves with low spatial resolution. The QB model provides excellent range reconstruction accuracy of <0.16 mm in the case of a simulated detector with sheets 0.1 mm thick (Kelleter and Jolly 2020). However, the sheets in the range telescope—and therefore the spatial resolution—are 2–3 mm thick. As such, the quenched Bragg curve is not directly fitted to the depth-light curve but integrated in segments that match the thickness of each sheet: the integrated bins are then used to fit the PDL curves from the range telescope. This method enables a partial compensation of the lower spatial resolution and improves the range fit accuracy to < 0.2 mm.

Table 1 lists the parameters used in the quenched Bragg curve fit. The density ρ is the density of water since the depth was converted to water equivalent depth before fitting. The parameters α, p, β and γ were obtained from Bortfeld's publication (Bortfeld 1997), which also contains an in-depth explanation of each parameters. For the quenched Bragg fit to the PDL curve, R_0, σ, Φ_0 and kB are used as fit parameters, where σ represents the peak width, Φ_0 stands for the proton fluence and kB is Birks' constant (Kelleter and Jolly 2020). All remaining model parameters are fixed during the fitting. The quenched Bragg model is implemented using the software toolkit ROOT (Brun and Rademakers 1997). Curve fitting is performed with the standard ROOT fit algorithm (Pearson χ^2 test) (Brun and Rademakers 2018).

The quenched Bragg curve and Bortfeld's Bragg curve model utilise the same parameters. One can therefore use the parameters fitted to the PDL curve as an input for Bortfeld's Bragg curve in order to reconstruct the original depth-dose curve as described in (Kelleter and Jolly 2020)f>.

2.7. Reference PDD curves at HIT

The reconstructed PDD curve is compared to a reference PDD curve in order to assess the goodness of the reconstruction for the experimental data taken at HIT. These reference PDD curves have been simulated in Fluka (Battistoni *et al* 2016) and benchmarked against ionisation chamber measurements (Parodi *et al* 2012). An offset of -3.05 ± 0.10 mm is applied to the reference curves to account for the water-equivalent path length (WEPL) from the exit of the vacuum chamber to the beam isocentre (Heeg 2019). The reference range

Table 1. Values of parameters used in the quenched Bragg curve fit. Table adapted from table 1 in (Bortfeld 1997)f>.

Variable	Description	Value	Unit
p	Exponent of range-energy relation	1.77[1997]	1
α	Proportionality factor	0.022[1997]	mm MeV^{-p}
β	Slope parameter of fluence reduction	0.001 2[1997]	mm^{-1}
γ	Fraction of locally absorbed energy	0.6[1997]	1
ρ	Density of water	1.0	g cm^{-3}
S	Scintillation light constant	9 744[1997]	photons MeV^{-1}
R_0	Proton beam range	fit parameter	mm
σ	Width of Gaussian range straggling	fit parameter	mm
Φ_0	Fluence factor	fit parameter	particlesmm^{-2}
kB	Birks' constant	fit parameter	mm MeV^{-1}

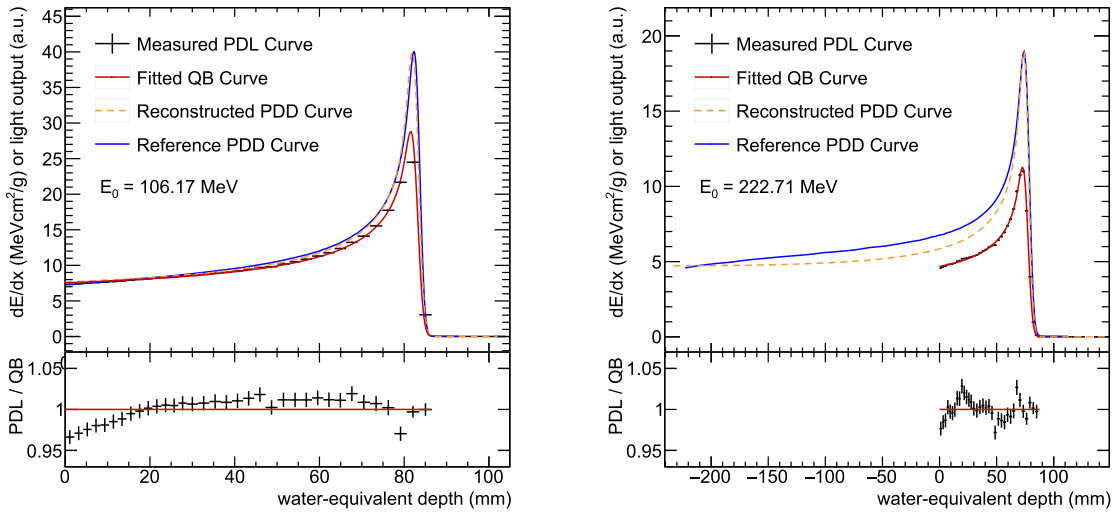

(a) 106.17 MeV (b) 222.71 MeV

Figure 3. Quenched Bragg curve fit to proton PDL curves and corresponding Bragg curve reconstruction with comparison to reference PDD curves for two beam energies. The 222.71 MeV data includes a PMMA degrader of 232.87 mm WET upstream of the range telescope, hence the missing data.

is defined as the 80% distal dose fall-off of a reference PDD curve. The maximum deviation from measured beam ranges is given as 0.2 mm (Parodi *et al* 2012), which includes the uncertainty on the WEPL to the isocentre and the reproducibility of the proton beam.

3. Results

3.1. Proton range measurement

The quenched Bragg curve described in section 2.6 has been fitted to 32 PDL curves with proton energies ranging from 48.45 MeV to 222.71 MeV. The fit range ends shortly after the Bragg peak since the QB model does not include the dose deposition from neutral particles which dominate beyond the Bragg peak. Figure 3 shows two examples of such a fit for proton beams of 106.17 MeV and 222.71 MeV, respectively. The subplots below show the percentage residuals of the QB curve fit. For 222.71 MeV, a total of 232.87 mm WET PMMA degrader was placed upstream of the range telescope in order to shift the Bragg peak into the range telescope. The WET of these PMMA degraders was measured with a PTW Peakfinder water column by measuring the range pull-back of a carbon beam which was chosen because of its narrower peak.

Alongside the measured PDL curve and resulting quenched Bragg curve fit, the reconstructed PDD curve as well as a reference PDD curve are also plotted. The reconstructed PDD curve is Bortfeld's Bragg curve model plotted with the parameters determined by the QB curve fit. The reference PDD curve is a

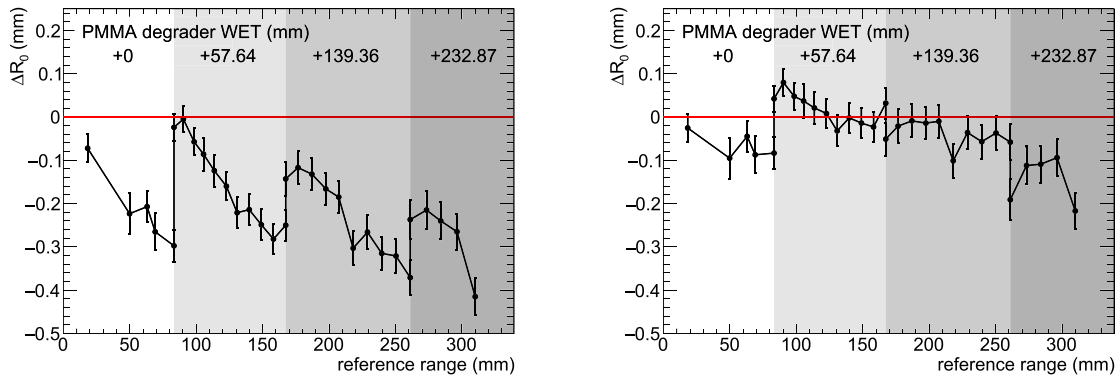

(a) No correction (b) With correction

Figure 4. Range difference ΔR_0 between the reconstructed proton range and the reference range. The gray sections highlight where different amounts of PMMA degrader have been used. The error bars show only the fit uncertainty. (a) shows the ΔR_0 without any corrections applied. (b) shows the same plot with a corrected scintillator stack WET of 127.6 mm, corresponding to a rotation of 4° relative to the beam axis.

benchmarked Fluka simulation (Parodi *et al* 2012). The reconstructed PDD curve is normalised such that its peak has the same magnitude as the reference PDD curve. The measured PDL curve is normalised such that its value at zero depth equals the first value of the reference PDD curve.

The quenched Bragg curve describes the measured PDL well for both beam energies: the difference is always smaller than 5%, which can be seen in the percentage residuals of figure 3. This quality of fit was also seen for the other measured ranges (not shown).

Furthermore, the reconstructed PDD curve and the reference PDD curve show good overall agreement (within $\pm$ 15%). Discrepancies can be seen in the plateau upstream of the Bragg peak and the dose build-up region. These stem from the coarse model of nuclear reactions applied in Bortfeld's analytical description of a Bragg curve (Bortfeld 1997). These discrepancies increase with increasing beam energy because the dose contribution of nuclear reactions increases with increasing beam energy (Newhauser and Zhang 2015).

In order to assess the accuracy of the range reconstruction, the reconstructed proton range is compared with the reference proton range: this is defined as the 80% fall-off of the distal edge of the reference proton curve. The uncertainty on the reference ranges is estimated to be 0.2 mm. Figure 4 shows the difference ΔR_0 between the measured range and the reference range, plotted versus the reference range. Different shades of gray highlight the use of different thicknesses of PMMA degrader which are given at the top of the plot. The red horizontal line marks the reference range. The error bars represent the uncertainty only on the quenched Bragg model fit. A discussion of other sources of uncertainty can be found in section 4.1.

It can be seen that the range reconstruction accuracy is between 0 mm and -0.41 mm. Steps in the range difference can be seen when new PMMA degraders are introduced in the beam path. ΔR_0 is also seen to monotonically decrease with increasing depth in the scintillator stack (saw tooth pattern in figure 4(a)). This indicates a potential underestimation of the actual WET of the scintillator stack. A larger effective WET of the stack could be explained by a small rotation of the stack during measurements i.e. that the stack was not correctly aligned to the beam. Figure 4(b) shows the range difference after the introduction of a rotation of the scintillator stack of 4° during the range measurement, resulting in a 0.26% increase in WET. This rotation was performed in post-processing by increasing the value of the stack WET. This correction largely removes the depth-dependence of ΔR_0. The influence of a potential rotation is discussed further in section 4.1.

3.2. Degrader WET

The range pull-back of different PMMA degraders is measured with the range telescope and compared to the range pull-back measured by a PTW Peakfinder. Six PMMA degraders with nominal water-equivalent thicknesses between 1.12 and 59.00 mm are investigated. The displaced air by the degraders is taken into account in the calculation of the WET. The difference between the WETs measured by each method is shown in figure 5 for assumed scintillator stack WETs of 127.27 mm and 127.6 mm, the latter taking into account a potential detector rotation of 4° relative to the beam axis. The difference between the measured degrader WET and the reference WET is below 0.1 mm when the stack rotation correction is included.

3.3. Beam spot position

A proton beam with an energy of 116.39 MeV was delivered 20 mm to the left and right of the central axis of the scintillator, at the same vertical distance to the CMOS sensor: the measured PDL curves are shown in

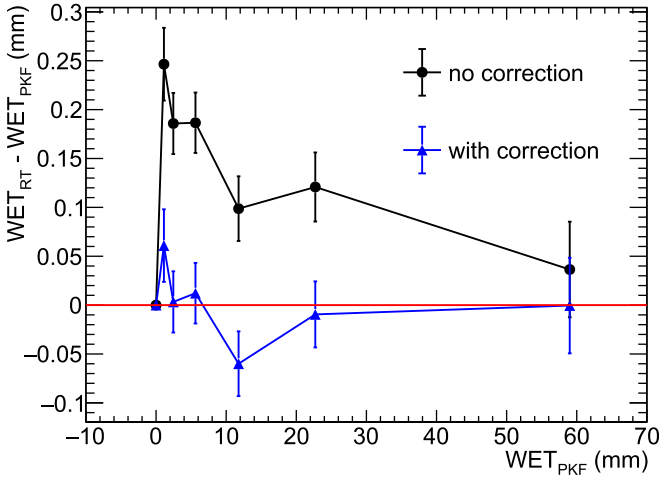

Figure 5. Difference between the PMMA degrader WET measured by the Peakfinder (PKF) and the range telescope (RT): 'no correction' refers to the measurement performed with an assumed WET of the scintillator stack of 127.27 mm and 'with correction' is for a detector WET of 127.6 mm, corresponding to a rotation of 4° relative to the beam axis.

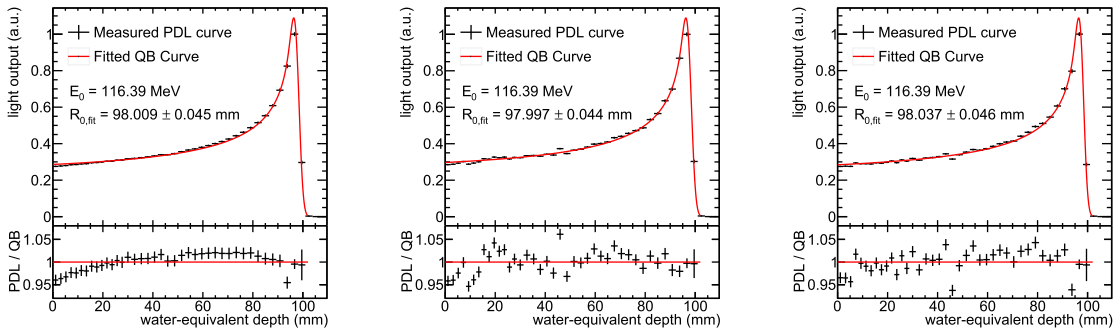

(a) Central beam position (b) 20 mm to the left (c) 20 mm to the right

Figure 6. Influence of the beam spot position on the light output. (a) central beam spot, (b) beam spot shifted 20 mm to the left (beam's eye view) and (c) beam spot shifted 20 mm to the right. $R_{0,fit}$ is given with fit uncertainty only.

figure 6. The same averaged ST curve is used for the light calibration of the three curves. The different spot position between calibration ST and measurement introduces noise as can be seen by comparing figure 6(a) with 6(b) and (c). Variations in the light output in a sheet of up to 7% are observed. These variations could be avoided by repeating the calibration shoot-through measurement at the respective spot position. Another possibility would be to use more reflective material such as Mylar foil for the wrapping of the sheets in order to reduce the transverse position-dependence of the light output. However, the observed variation in range is below 0.04 mm which is within the fit uncertainty on the range measurement. It can be concluded that the beam range measurement is robust against small horizontal offsets from the central axis. Simulations suggest that this is also the case for small vertical beam offsets; however, this was not verified experimentally. The results also set a limit to the influence of the non-uniformity in the sheet thickness ($\pm$ 0.02 mm) on the beam range measurements. Such non-uniformity would show up as a position-dependent beam range, which is shown to be lower than 0.04 mm.

3.4. Beam spot size

A proton beam with an energy of 120.97 MeV was delivered to the range telescope with six different spot sizes ranging from 13.4 to 20.9 mm full-width half-maximum (FWHM). The PDL curves for spot sizes of 13.4, 16.5 and 20.9 mm are shown in figure 7. The maximum difference in light output between specific sheets is found to be 2%. However, the range reconstruction produces nearly identical results for all different spot sizes with a maximum range difference of < 0.05 mm. It is therefore concluded that it is possible to measure the range of a proton pencil beam with the range telescope independent of the beam spot size and without adapting the beam spot size of the calibration ST. The result also shows that the range measurement is robust against the beam widening due to multiple scattering as the protons slow down in the scintillator stack.

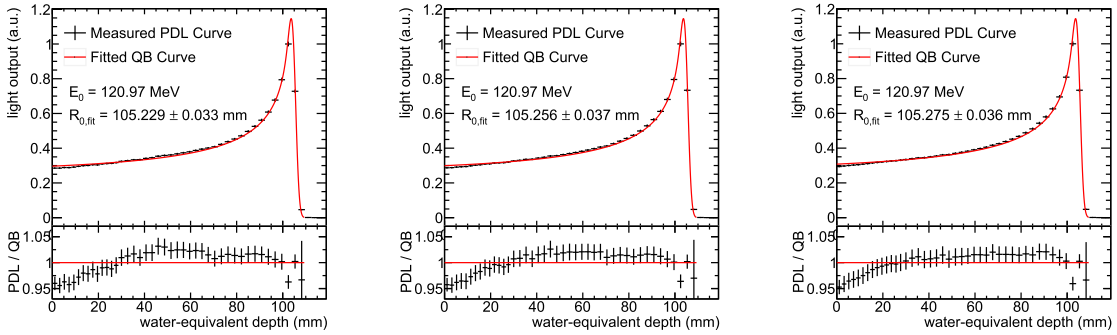

(a) Spot size: 13.4 mm (b) Spot size: 16.5 mm (c) Spot size: 20.9 mm

Figure 7. Influence of the beam spot size on the light output. (a) Beam spot size of 13.4 mm FWHM, (b) 16.5 mm and (c) 20.9 mm. $R_{0,fit}$ is given with fit uncertainty only.

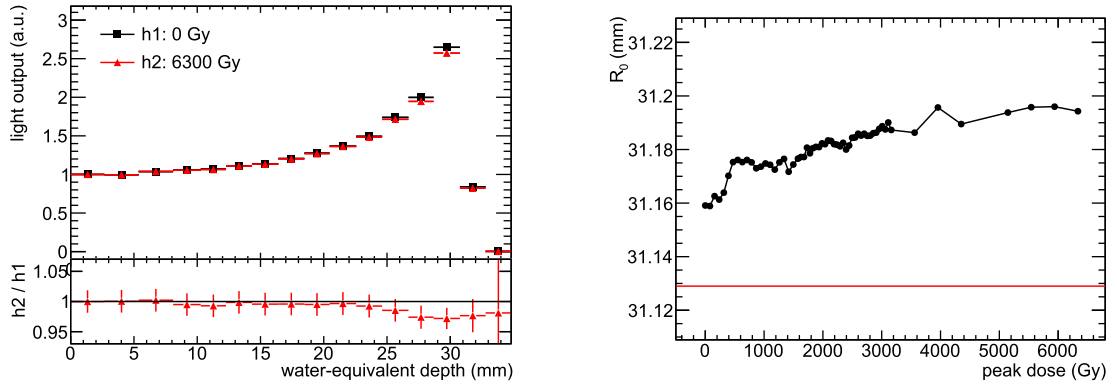

(a) Depth-light curve before/after irradiation (b) Range evolution with dose

Figure 8. (a) Depth-light curve before and after delivering 6,300 Gy peak dose to the scintillator. (b) Evolution of reconstructed range as a function of the delivered dose at the Bragg peak.

3.5. Radiation hardness

A major disadvantage of plastic scintillator is that it suffers from a reduction in scintillation light output as a result of radiation damage. It is therefore important to investigate the impact of large amounts of absorbed dose on the detector performance. Experiments to determine the radiation hardness of the detector were carried out at the Clatterbridge Cancer Centre using a collimated double-scattered proton beam with a beam energy of 60 MeV and a reference range of (31.13 ± 0.20) mm in water. A total dose of 6,300 Gy was delivered to the range telescope with measurements of the light output taken at regular intervals during the irradiation. The dose per image frame was $\approx$ 83 mGy.

Figure 8(a) shows two measured PDL curves before and after irradiation. The two curves are normalised to the light output in the first sheet because of the fluctuating beam intensity. It can be seen that there is a small reduction of the light output at the Bragg peak of ~ 3% following the irradiation. Figure 8(b) shows the evolution of the measured range over the course of the radiation hardness assessment. A red horizontal line indicates the value of the reference range. The effect of the peak reduction due to radiation damage can be observed as a small steady increase in the measured beam range. The observed range increase during irradiation is 0.04 mm. The range uncertainty for the Clatterbridge measurements is the same as for the measurement at HIT for a beam range of 31.13 mm (see section 4.1). However, the error bars are not shown in figure 8(b) in order not to overload the plot. The impact of the observed radiation damage is discussed in section 4.2. No radiation damage to the CMOS sensor or the readout electronics was observed.

3.6. Ion beams

The range telescope was tested with multiple different ion species available at the HIT facility including helium, carbon and oxygen ions. Figure 9 shows four PDL curves of these ions at approximately the same beam range. The curves are normalised to the light output in the first sheet. While the Bragg peak becomes sharper with increasing ion charge, the observed peak-to-plateau ratio in the depth-light curve decreases. This is likely the result of the strong quenching that the ions undergo due to their high specific energy loss as

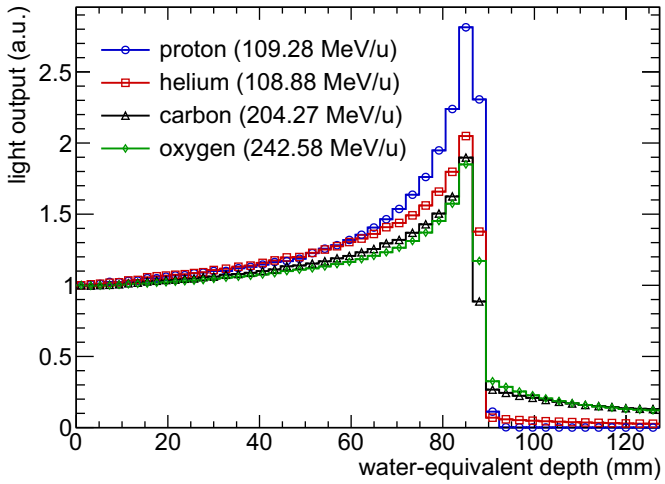

Figure 9. Comparison of different ion beams with approximately the same range in the range telescope.

Table 2. Beam range uncertainty sources split up into different beam range sections. (*) is the quadratic sum without misalignment- and degrader-related uncertainties.

	Range uncertainty (mm)			
Beam range (mm)	18–83	83–170	170–260	260–310
Fit uncertainty	0.04	0.04	0.04	0.04
Stopping power ratio	0.05–0.15	0.05–0.15	0.05–0.15	0.05–0.15
QB model	0.2	0.2	0.2	0.2
Calibration ST	0.04–0.16	0.03–0.27	0.04–0.39	0.05–0.14
Stack WET (PKF)	0.01–0.03	0.01–0.03	0.01–0.04	0.01–0.02
Stack WET (rotation)	0.04–0.2	0.06–0.27	0.07–0.30	0.07–0.19
Degrader WET	0	0.04	0.08	0.14
Quadratic sum	0.22–0.36	0.22–0.46	0.24–0.56	0.27–0.37
Quadratic sum*	0.21–0.25	0.21–0.26	0.21–0.26	0.21–0.25

well as the low spatial resolution of the detector which suppresses the tighter peak. As expected, the light production in the fragmentation tail is seen to increase with increasing atomic number of the projectile. The range of the ion beams has not been evaluated because of the lack of an analytical description of the ion PDL curve at the present day. The development of an analytical function for the ion beam Bragg curve which includes the projectile fragmentation is part of future work.

4. Discussion

4.1. Range uncertainty

All identified range uncertainty sources are listed and quantified in table 2.

4.1.1. Degrader WET

A rotation uncertainty on the placement of the PMMA degraders of 2° relative to the beam direction is realistic—either during degrader characterisation or range measurement—which results in an uncertainty on the degrader WET and thus the proton range of up to $\pm$ 0.14 mm. This uncertainty is caused by the difficulty of aligning a small piece of PMMA perpendicular to the laser positioning system and the uncertainty of the laser system itself.

4.1.2. Stack WET (PKF)

The uncertainty associated with the measurement of the scintillator stack WET with the Peakfinder is $\pm$ 0.04 mm. This uncertainty was determined by repeating the measurement of the range pull-back. It translates into a range uncertainty of $\pm$ 0.01–0.04 mm.

4.1.3. Stack WET (rotation)
A rotation of the scintillator stack of up to 4° relative to the beam axis during the measurement of PDL curves is realistic, which amounts to a stack WET uncertainty of ± 0.3 mm. This translates into a range uncertainty of ± 0.04–0.3 mm, depending on the depth of the proton beam in the scintillator. The uncertainty is larger than the one for the PMMA degrader alignment because it is not the scintillator stack itself but the light-tight enclosure that is aligned with the laser system. Figure 4(b) shows the range difference when the scintillator stack is rotated by 4° relative to the beam axis. It can be seen that the negative slope in each section of the plot becomes more flat and the steps in the range due to the uncertainty on the degrader WET are easier to identify. This is a hint that the scintillator stack was indeed misaligned with the beam direction by a rotation of approximately 4° during the range measurement.

4.1.4. Calibration ST
A potential rotational misalignment of the scintillator stack during the shoot-through measurement would result in a depth-dependent distance between CMOS sensor and the central beam axis, leading to an averaged ST curve that has a systematic error. When the light calibration is performed with an averaged ST curve that has a rotational misalignment, an artificial slope would be introduced into the PDL curve. The effect on the light output of a stack rotation of 4° is estimated by the means of a Geant4 (Agostinelli *et al* 2003, Allison *et al* 2006, Allison *et al* 2016) simulation. The QB model is then fitted to the PDL curve with and without the simulated correction in order to determine the effect on the range reconstruction. The effect on the range measurement is found to be ± 0.03–0.39 mm.

4.1.5. Quenched Bragg model:
The QB model was shown in simulation to always reproduce the reference proton range within 0.2 mm for proton beam energies between 60–240 MeV and a spatial resolution of 3 mm. This systematic deviation can be explained by the lack of an appropriate description of nuclear reactions in Bortfeld's Bragg curve model (Bortfeld 1997).

4.1.6. Stopping power ratio
The water-equivalent thickness of the scintillator depends on the beam energy with which it is probed due to the variation in stopping power ratio (SPR) of water and polystyrene. This effect is quantified using the SPR data for water and polystyrene availaible from the NIST database (Berger *et al* 2017). The effect on the proton range was found to be ± 0.05–0.15 mm, depending on the depth of the proton beam in the scintillator stack.

4.1.7. Fit uncertainty
The uncertainty on the fitted range parameter, R_0 that is returned by the minimisation process is approximately ± 0.04 mm, independent of the beam range. Its value depends on the uncertainty of the light output in each scintillator sheet.

The dominant range uncertainties mentioned above are caused not by the range telescope detection technique itself but either by poor detector alignment (rotation uncertainty) or the use of PMMA degraders. Range uncertainties inherent to the range telescope are the fit uncertainty, the QB model uncertainty and the stopping power ratio. If the external range uncertainties are reduced—e.g. by improving the detector alignment or by avoiding the use of PMMA degraders—the range uncertainty could be reduced to approximately ± 0.26 mm (see bottom line in table 2). One of the dominant range uncertainties would then be the stopping power ratio which could be corrected for using the SPR tables in the NIST database.

4.2. Radiation damage
The radiation damage measurements described in section 3.5 show that 6,300 Gy of integrated dose leads to a relative reduction of the light output of 3% at the Bragg peak compared to the entrance. The resulting impact on the range reconstruction is found to be 0.04 mm at a range in water of 31.13 mm: this is well within the uncertainty on the range measurement presented above (± 0.21 mm) and the reference range (± 0.2 mm). At an assumed entrance dose rate of 0.25 Gy s^{-1} (the typical clinical entrance dose rate at Clatterbridge Cancer Centre) a beam spot measurement with a typical duration of 10 ms (van de Water *et al* 2015) would deliver an entrance dose of 0.002 5 Gy to the detector. In order to see a scintillator damage comparable to the one in figure 8(a) after delivering 6,300 Gy peak dose, about 500, 000 beam measurements would need to be performed (peak-to-entrance dose ratio of 4.7 at CCC). Furthermore, the light output of the detector can easily be recalibrated following the procedure described in section 2.5 which would correct for any radiation damage. The detector is therefore believed to be able to deliver long-term reliable range measurements at clinical proton dose rates.

4.3. Comparison with other range detectors

The main disadvantages of the scintillator-based range telescope are the radiation damage, the low spatial resolution and the sensitivity to misalignment. The first two are found to be manageable by occasional re-calibration and the use of a bespoke range reconstruction algorithm. An updated prototype detector will require a positioning system that reduces the detector alignment uncertainty to below 2°.

A major advantage of the scintillator is that it has a density similar to that of water which facilitates the direct measurement of water-equivalent depth compared with multi-layer ionisation chambers. The detector does not require high voltage for operation and unlike ionisation chambers its light output is independent of the dose rate. This is important for high dose-per-pulse beams (FLASH proton therapy) for which ionisation chambers have been shown to have a dramatically reduced ion collection efficiency (Petersson *et al* 2017).

Thanks to the absence of a lens, no depth-dependent correction factors need to be applied to the measured light output as is the case for monolithic scintillation detectors with a single camera. The compact and lightweight design would enable the detector to be mounted to the beam nozzle such that one could easily perform range measurements at different gantry angles.

It is of note that the quenched Bragg curve utilised for fitting does not require simulations of the LET distribution in the scintillator in order to correct for the light quenching. Instead, both the LET distribution and the quenching correction are fitted simultaneously, thus avoiding a potential mismatch between the two. The range reconstruction uncertainty without PMMA degraders and with improved detector alignment would be on the order of $\pm$ 0.26 mm. Comparable commercial detectors such as the IBA Giraffe have a range reconstruction uncertainty of 0.5 mm (Baeumer *et al* 2015). Furthermore, the range telescope is shown to be able to cope with proton beams of different spot sizes as well as off-axis beams which is important if scanned beams shall be measured without moving the detector.

4.4. Applications in particle therapy

Initially, the detector was designed to perform range quality assurance measurements of proton pencil beams. However, the detector is also suitable for measuring the WET of any beam degrader material, immobilisation devices or samples of implants that can be found in the beam path. Furthermore, it could be used as the range measurement stage in a patient-specific QA detector. For this, the light readout would need to be faster in order to allow the measurement of single beam spots. Routes towards faster light readout are discussed in section 4.5.

In addition, the range telescope could be used for the measurement of the residual range of a beam that passes through a patient, either using patient range probing (Mumot *et al* 2010) or in a potential mixed helium/carbon beam (Mazzucconi *et al* 2018, Volz *et al* 2020). This would enable the detection of inter- or intra-fractional movements of the tumour: for further discussion see (Volz *et al* 2020).

There is also the potential of using the range telescope for range QA measurements of ion beams. However, more work would need to go into the development of a quenched Bragg curve model for ion beams that also takes into account dose deposition from beam fragmentation in order to achieve a clinically relevant range reconstruction accuracy.

4.5. Future work

A large range uncertainty is currently the use of PMMA degraders, which were necessary with the existing setup to measure the full range of clinical particle beam energies due to the limited WET of the scintillator stack. Furthermore, the large-scale CMOS sensor offers a two-dimensional resolution that is not necessary for range measurements whilst being fragile and delicate to handle. Future work will therefore focus on developing a full-scale range telescope (WET $\approx$ 30 cm) with a custom light-detection system based on photodiodes. In this new setup, each scintillator sheet will be coupled to a single photodiode. Custom-built readout electronics will allow the range telescope readout to be synchronised with the beam delivery for an automated data acquisition. This new system will also be faster than the current light readout and therefore allow the measurement of individual beam spots that take on the order of milliseconds to be delivered.

A potential upgrade of the detector with another system for making 2D beam spot and position measurements upstream of the scintillator stack for quasi-3D beam measurements is also being considered.

5. Conclusion

A novel range telescope based on plastic scintillator sheets and a CMOS image sensor readout has been developed and tested with clinical proton beams. The proposed design avoids optical artefacts that are common in scintillation detectors. The maximum range difference between measurement and reference is -0.41 mm at a beam range of 310 mm. The difference is smaller if no PMMA degraders are used and a potential rotation of the detector during the measurements is taken into account. The water-equivalent

thickness of different PMMA degraders is reconstructed within ± 0.1 mm in range pull-back measurements. This accuracy is achieved with a bespoke image analysis and range reconstruction algorithm that simultaneously fits the LET distribution and the quenching correction along the proton path in the scintillator. A radiation hardness evaluation demonstrates that the scintillator has the capability to fulfil the longevity requirements in a clinical proton therapy centre by showing only 3% light output reduction following a dose deposition worth about 500, 000 beam spot measurements, with a change in measured range well within the uncertainty of the detector range measurement. The range reconstruction accuracy is also insensitive to small changes in the beam spot size, the lateral beam position within the detector and the initial particle energy. Range measurements of ion beams are also possible but require the development of a new depth-light curve model in order to achieve a similar range reconstruction accuracy compared with protons.

Acknowledgments

The authors would like to thank the operators and scientists at HIT and Dr Andrzej Kacperek from the Clatterbridge Cancer Centre for the support during the beam tests at their facilities. This project has received funding from the European Union's Horizon 2020 research and innovation programme under the Marie Sklodowska-Curie Grant No. 675265. The authors have no relevant conflicts of interest to disclose.

ORCID iDs

Laurent Kelleter https://orcid.org/0000-0003-4346-9741
Raffaella Radogna https://orcid.org/0000-0002-1094-5038
Lennart Volz https://orcid.org/0000-0003-0441-4350
Simon Jolly https://orcid.org/0000-0002-2713-0732

References

Actis O, Meer D, Koenig S, Weber D C and Mayor A 2017 A comprehensive and efficient daily quality assurance for PBS proton therapy *Phys. Med. Biol.* **62** 1661–75
Agostinelli S *et al* 2003 GEANT4–a Simulation toolkit *Nucl. Instrum. Methods* A **506** 250–303
Allison J *et al* 2006 Geant4 developments and applications *IEEE Trans. Nucl. Sci.* **53** 270–8
Allison J *et al* 2016 Recent developments in Geant4 *Nuclear Instrum. Methods Phys. Res. Sect.* A **835** 186–225
Almurayshid M, Helo Y, Kacperek A, Griffiths J, Hebden J and Gibson A 2017 Quality assurance in proton beam therapy using a plastic scintillator and a commercially available digital camera *J. Appl. Clin. Med. Phys.* **18** 210–9
Alsanea F, Darne C, Robertson D and Beddar S 2020 Ionization quenching correction for a 3D scintillator detector exposed to scanning proton beams *Phys. Med. Biol.* **65** 075005
Archambault L, Poenisch F, Sahoo N, Robertson D, Lee A, Gillin M T, Mohan R and Beddar S 2012 Verification of proton range, position and intensity in impt with a 3D liquid scintillator detector system *Med. Phys.* **39** 1239–46
Baeumer C, Koska B, Lambert J, Timmermann B, Mertens T and Talla P T 2015 Evaluation of detectors for acquisition of pristine depth-dose curves in pencil beam scanning *J. Appl. Clin. Med. Phys.* **16** 151–63
Battistoni G *et al* 2016 The FLUKA code: an accurate simulation tool for particle therapy *Front. Oncol.* **6** 116
Beaulieu L and Beddar S 2016 Review of plastic and liquid scintillation dosimetry for photon, electron and proton therapy *Phys. Med. Biol.* **61** R305
Beddar S, Archambault L, Sahoo N, Poenisch F, Chen G T, Gillin M T and Mohan R 2009 Exploration of the potential of liquid scintillators for real-time 3D dosimetry of intensity modulated proton beams *Med. Phys.* **36** 1736–43
Berger M J, Coursey J S, Zucker M A and Chang J 2017 Stopping-Power and range tables for electrons, protons and helium ions *NIST Standard Reference Database 124*
Birks J B 1951 Scintillations from organic crystals: specific fluorescence and relative response to different radiations *Proc. Phys. Soc.* A **64** 874
Boon S N, van Luijk P, Schippers J M, Meertens H, Denis J M, Vynckier S, Medin J and Grusell E 1998 Fast 2D phantom dosimetry for scanning proton beams *Med. Phys.* **25** 464–75
Bortfeld T 1997 An analytical approximation of the Bragg curve for therapeutic proton beams *Med. Phys.* **24** 2024–33
Brun R and Rademakers F 1997 ROOT: An object oriented data analysis framework *Nucl. Instrum. Methods* A **389** 81–6
Brun R and Rademakers F 2018 ROOT User's Guide 6 https://root.cern.ch/root/htmldoc/guides/users-guide/ROOTUsersGuide.html Accessed on 2019-11-21
Darne C D, Alsanea F, Robertson D G, Sahoo N and Beddar S 2018 Performance characterization of a 3D liquid scintillation detector for discrete spot scanning proton beam systems *Phys. Med. Biol.* **62** 5652–67
Fukushima Y, Hamada M, Nishio T and Maruyama K 2006 Development of an easy-to-handle range measurement tool using a plastic scintillator for proton beam therapy *Phys. Med. Biol.* **51** 5927–36
Gillin M T *et al* 2010 Commissioning of the discrete spot scanning proton beam delivery system at the University of Texas M.D. Anderson Cancer Center, Proton Therapy Center, Houston *Med. Phys.* **37** 154–63
Grevillot L *et al* 2018 Implementation of dosimetry equipment and phantoms at the MedAustron light ion beam therapy facility *Med. Phys.* **45** 352–69
Heeg P 2019 Private communication
Hoehr C, Lindsay C, Beaudry J, Penner C, Strgar V, Lee R and Duzenli C 2018 Characterization of the exradin W1 plastic scintillation detector for small field applications in proton therapy *Phys. Med. Biol.* **63** 095016
Karger C P, Jäkel O, Palmans H and Kanai T 2010 Dosimetry for ion beam radiotherapy *Phys. Med. Biol.* **55** R193–234

Karsch L, Beyreuther E, Burris-Mog T, Kraft S, Richter C, Zeil K and Pawelke J 2012 Dose rate dependence for different dosimeters and detectors: TLD, OSL, EBT films and diamond detectors *Med. Phys.* **39** 2447–55

Kelleter L and Jolly S 2020 A mathematical expression for depth-light curves of therapeutic proton beams in a quenching scintillator *Med. Phys.* **47** 2300–08

Kelleter L, Zhen Hong Tham B, Saakyan R, Griffiths J, Amos R, Jolly S and Gibson A 2019 Technical Note: Simulation of dose buildup in proton pencil beams *Med. Phys.* **46** 3734–8

Knoll G F 1979 *Radiation Detection and Measurement* (Hoboken, NJ: Wiley)

Kristensen I, Nilsson K and Nilsson P 2015 Comparative proton and photon treatment planning in pediatric patients with various diagnoses *Int. J. Particle Therapy* **2** 367–75

Mazzucconi D, Agosteo S, Ferrarini M, Fontana L, Lante V, Pullia M and Savazzi S 2018 Mixed particle beam for simultaneous treatment and online range verification in carbon ion therapy: Proof-of-concept study *Med. Phys.* **45** 5234–43

Mumot M, Algranati C, Hartmann M, Schippers J M, Hug E and Lomax A J 2010 Proton range verification using a range probe: definition of concept and initial analysis *Phys. Med. Biol.* **55** 4771–82

Newhauser W D and Zhang R 2015 The physics of proton therapy *Phys. Med. Biol.* **60** R155–209

NuviaTech Instruments 2019 *NuDET Plastic: Specification Sheet*

Parodi K, Mairani A, Brons S, Hasch B G, Sommerer F, Naumann J, Jäkel O, Haberer T and Debus J 2012 Monte Carlo simulations to support start-up and treatment planning of scanned proton and carbon ion therapy at a synchrotron-based facility *Phys. Med. Biol.* **57** 3759–84

Particle Therapy Co-Operative Group 2019 Particle therapy facilities in clinical operation www.ptcog.ch/index.php/facilities-in-operation Accessed on 2019-08-07

Petersson K, Jaccard M, Germond J-F, Buchillier T, Bochud F, Bourhis J, Vozenin M-C and Bailat C 2017 High dose-per-pulse electron beam dosimetry - a model to correct for the ion recombination in the advanced markus ionization chamber *Med. Phys.* **44** 1157–67

Rana S, Bennouna J, Samuel E J J and Gutierrez A N 2019 Development and long-term stability of a comprehensive daily QA program for a modern pencil beam scanning (PBS) proton therapy delivery system *J. Appl. Clin. Med. Phys.* **20** 29–44

Robertson D, Hui C K, Archambault L, Mohan R and Beddar S 2014 Optical artefact characterization and correction in volumetric scintillation dosimetry *Phys. Med. Biol.* **59** 23–42

Robertson D, Mirkovic D, Sahoo N and Beddar S 2013 Quenching correction for volumetric scintillation dosimetry of proton beams *Phys. Med. Biol.* **58** 261–73

Russo S*et al* 2017 Characterization of a commercial scintillation detector for 2-D dosimetry in scanned proton and carbon ion beams *Phys. Medica* **34** 48–54

Subrahmanyam H N and Subramanyam S V 1987 Thermal expansion of irradiated polystyrene *J. Mater. Sci.* **22** 2079–82

van de Water S, Kooy H M, Heijmen B J M and Hoogeman M S 2015 Shortening delivery times of intensity modulated proton therapy by reducing proton energy layers during treatment plan optimization *Int. J. Radiat. Oncol. Biol. Phys.* **92** 460–8

Volz L*et al* 2020 Experimental exploration of a mixed helium/carbon beam for online treatment monitoring in carbon ion beam therapy *Phys. Med. Biol.* 65 055002